SOME RESULTS ON HADRON PRODUCTION IN INELASTIC μp AND ep SCATTERING EXPERIMENTS AT THE STANFORD LINEAR ACCELERATOR LABORATORY.

J. Ballam, SLAC
Stanford, California

Introduction

There are four separate inelastic lepton scattering experiments, either completed or in progress at SLAC. These are

1. $\mu^- p \rightarrow \mu^- +$ hadrons (Fast cycling HBC)
2. $e^- p \rightarrow e^- +$ forward hadrons (wide angle spectrometer).
3. $\mu^+ p \rightarrow \mu^+ +$ hadrons (streamer chamber)
4. $e^+ e^- \rightarrow$ hadrons (SPEAR colliding beams).

I will report on the main features of reactions 1) and 2). There is no date to report from 3) and 4) although both hare had successful runs.

Fig. 1a describe briefly the kinematical variables used in the analysis q there experiments and Fig. 1b relates the space-like and time-like aspects of there processes through the $Q^2 = 0$ point (ordinary photoproduction).

The most studing features q there experiments may be summarized as follow:

a. Al fixed ν the average multiplicity seems to fall slowly with Q^2
b. Al high Q^2 the hadronic charge ratio (+/-) increases with positive values of the Feynman $x \simeq P_e^*/P_{MAX}^*$
c. σ_L/σ_T for ρ^o electroproduction is ~ 0.5

I will discuss the following topics:

1. $\dfrac{\sigma(1,3,5,7)\ \text{charged prongs}}{\sigma_{Tot}}$ as $f(W,Q^2)$

2. $\langle n \rangle$ as $f(Q^2)$ for fixed W, $\langle n \rangle$ is the average charged multiplicity

3. $\langle n \rangle$ as $f(W)$ for all Q^2.

4. Exclusive processes (Vector meson Electroproduction)

$$\gamma_v + p \rightarrow \rho^o + p$$
$$\rightarrow \omega + p$$
$$\rightarrow \varphi + p$$

(Published in Proceedings of the IV International Symposium on Multiparticle Hadrodynamics, Pavia (Collegio Ghislieri), 31st August - 4th September 1973)

5. (+/-) ratios as $f(x, Q^2)$ for $\gamma_\nu + p \to h^\pm$
$\gamma_\nu + n \to h^\pm$

6. Inclusive processes

$$\gamma_\nu + p \to p + X$$
$$\to \pi^\pm + X$$

The work done on reaction 1) has been reported at the Bonn Conference(1,2,3) Aug. 1973 and that of reaction 2 appears in several publications(4,5,6).

Experimental Apparatus.

Fig. 2 shows schematically the beam configuration and the bubble chamber with its μ-detector. Incident electrons of energy 20 GeV impinged on a high Z target at the front of the beam transport. Muons were pair-produced in the first few radiation lengths of material. Negative muons were focussed on 3.7 meters of beryllium placed inside the first of 3 foci in the transport system. Dispersion in the beam at this point provided us with a $\Delta p/p = \pm 2\%$ momentum bite. The beryllium served to attenuate the fraction of hadronic particles in the beam through collisions, while the μ component of the beam suffered only loss of energy due to ionization.

Multiple scattering losses were minimized by placing the beryllium at a focus. By these means we obtained an essentially pure μ beam. The measured contamination from π's was $\pi/\mu = 0.5\times10^{-4}$.

Downstream of the first focus we placed collimators of iron and lead and substantial amounts of iron shielding at critical points. Proportional wire chambers were placed before the two downstream foci to aid in the accurate tuning of the beam. These efforts were necessary to guarantee e a beam at the bubble chamber which was contained within a well defined space.

The trigger counters and spark chambers downstream of the bubble chamber were sensitive to halo particles. Halo particles are a serious problem in muon beams, and to us were a potential source of false triggers, as well as unwanted tracks in our spark chambers. Our beam had a halo of 2% seen in the trigger counters behind the bubble chamber. Figure 1b shows the placement of counters before and after the bubble chamber. Veto counters placed directly in front of the bubble chamber eliminated halo μ's from the trigger. The beam was deflected upward by the bubble chamber magnetic field (26.2 Kgauss) and passed through windows and apertures in the iron. Behind the bubble chamber at a distance of about 3 meters from the center of the fiducial volume, we placed the μ detector, which extended another 2.4 meters. The beam passed through the center of this detector.Four iron blocks, each 12 inches thick, had beam apertures cut in them, and provided additional attenuation for π's in the beam which scatter in the bubble chamber and could trigger our system. Two banks of scintillation counters were placed such that they surrounded the beam. Fast coincidence between the forward and backward bands of scintillation provided the initial electronic trigger with tight time resolution and course spatial resolution. The spark chambers were triggered by this coincidence to give us a much better spatial resolution. The spark chamber data were recorded on magnetic tape. The scintillator hodoscope information was processed by a PDP-8 on-line computer looking at the hodoscope pattern and the final decision to trigger the camera was made during the remaining 2-3 millisecond portion of the bubble chamber expansion cycle.

TABLE I

Beam characteristics and Event Rate

μ^- beam	Event Rates		
$p = 16 \pm 0.6$ GeV/c	30×10^6	expansions	10/sec
I = 1000 's/sec	and 100	μ's/exp.	
Vert. size = 11 cm FWHM	94,000	triggered pictures	
Horiz.size = 1.2 cm FWHM	4,922	Useful events	
Penetrating halo < 2%	1,181	elastic	
π/μ contamination < $5\text{x}10^{-5}$	3,741	inelastic.	

Fig. 3a shows the distribution of the data in the variables W and Q^2. Events extend in W from elastic scattering at $W = M_p$ to W = 5.2 GeV and in Q^2 to values as large as 3.6 GeV^2. Elastic events are seen on the left. Enhancements in resonance regions are also apparent. The accumulation of events at low Q^2, high W occur due to the shape of our acceptance for scattered μ's. These events correspond to forward scattered μ's which lose considerable energy. The accumulation for such scatters is seen because the small Q^2 involved corresponds to relatively large cross sections, and the outgoing μ's energy is sufficiently low such that the magnetic field deflects them upward, our of the beam, into our trigger counters. We chose not to eliminate these events in the fast trigger, easily done by placing additional veto counters appropriately, so as not to complicate unnecessarily the shape of our acceptance.

The probability for detecting the scattered μ's depends on Q^2 and W of the μ as well as the geometry of the experiment, but is independent of the nature of the final state hadrons. We calculate this probability using a Monte Carlo simulation of the experiment. Contours of probability are shown superimposed on the data and indicate a maximum, approaching unity, for W=3 GeV and Q^2=1 GeV^2. Due to the rapidly decreasing flux of virtual photons and total μ cross section as the Q^2 of the process increases, the majority of the events fall at low Q^2 values. The low Q^2 cutoff is purposely introduced by detecting only those scattered μ's with angles $\gtrsim 1°$, while the decreasing probability at large Q^2 occurs because large angle scatters miss the outer edges of our trigger system. We estimate the accuracy of the Monte Carlo calculation to be within $\pm$ 10% relative error for the central regions where the probability is > .7; for the outer regions, where the probability is < .3, the errors increase the perhaps $\pm$ 30%. For the outer regions, the reduced acceptance probability is sensitive to the exact location of the outer edges of the counters giving rise to increased uncertainty.

In Figure 3b, we show the same data, but superimposed are contours for the scaling variable $\omega' = 1 + W^2/Q^2$, and ε the longitudinal to transverse polarization parameter.

The wide angle spectrometer.

The experimental apparatus consisted of a 19.5 GeV electron beam incident on a 4 cm liquid hydrogen target and a large aperture spectrometer to detect a large fraction of the forward final state particles with lab momenta greater than ~ 1 GeV/c. These elements are shown in Fig. 4 and discussed in greater detail below.

The electron beam contained typically 10^4 e^- per 1.5 μ sec long SLAC pulse. At the experimental target, the beam had an rms width of 0.5 mm x 0.5 mm and an rms divergence less than 0.2 mrad x x 0.2 mrad. There the beam was very well collimated, with fewer than 1 in 10^5 e^- outside a 0.5 cm diameter circle. The momentum spread in the beam was 0.2%.

The spectrometer magnet has 1.37 m diameter pole faces separated by 0.91 m. It was centered on the beam line, 2.54 m downstream from the target, with its principal field component horizontal. At the magnet center, this field was 10 kG and the field integral 17 kG-meters.

The unscattered beam and the forward electromagnetic backgrounds passed through the magnet in a field-free region created by a cylindrical superconducting tube[13]. Beyond the magnet were two optical spark chambers separated by 1.7 m. The chambers had inactive holes through their centers, where the beam tube passed. The apertures of the magnet, spark chambers, and beam tube produced the acceptance shown in Fig. 3.

The apparatus was triggered on the detection of a scattered electron by a hodoscope of 20 scintillation counters and 11 shower counters[14] behind the second spark chamber. The shower counter thresholds were set to $\sim$ 4 GeV. Photon triggers were eliminated by the requirement that a shower counter fire coincident with the scintillators in front of it. The kinematic range of inelastic electron scatters covered by this trigger was roughly $|q^2| > 0.3$ $(\mathrm{GeV/c})^2$, $\nu < 15$ GeV. There was no hadron requirement in the trigger.

For each trigger a single picture was taken of the optical spark chambers on 70 mm film. The camera was located in the horizontal plane 21.6 m from the beam line with its optic axis aligned perpendicular to the beam. Each picture contained four views of each chamber, a direct view, a top and a bottom view in small angle stereo, and a rear view to expose tracks blocked in the direct view by a beam pipe.

Charged multiplicities and Cross-section from the Hybrid Experiment

Experimental cross sections were obtained by monitoring of the beam. A scintillation counter was placed directly in the beam, large enough to contain the full beam. The output signal was integrated, digitized and accumulated in a scaler. Frequent and accurate calibration of the beam monitor was maintained by direct count of μ -tracks in the bubble chamber.
The error in the incident beam flux was estimated to be $\pm$ 5%.

The resulting values for $\sigma_T + \varepsilon \sigma_S$ are shown in Figures 6a-4d. We choose four bins in W: W=1.4 to 1.8, W=1.8 to 2.8, W=2.8 to 3.8, W=3.8 to 4.8. Corresponding to each of these bins in W, we present the Q^2 dependence of the cross section. For sake of comparison, we show the radiatively cor

rected electroproduction cross sections from SLAC[1] single arm data as a solid line.
In the inelastic regions, the agreement with e-p inelastic cross sections is satisfactory for the first three W bins, $1.4 \leq W \leq 2.8$ GeV. However in the upper W bin, $3.8 \leq W \leq 4.8$ GeV, the ratio to e-p cross sections falls to $\sim .7$.
However, these last points fall in a region of rapidly decreasing acceptance probability, which may lead to the discrepancy shown. Except for normalization, there appears to be good agreement in shape with the e-p data.
The fall-off of the cross section, as Q^2 increases, follows closely the e-p data. For the analysis of the hadron final states, the normalization of the data is unimportant. We show ratios (e.g., prong ratios, multiplicities, charge ratios) and all quantities are insensitive to changes in the acceptance probability.

Combining all our data, we obtain a ratio $\sigma(\mu p)/\sigma(ep) = .87 \pm .02$. In addition to the .02 statistical error, there are $\pm$ 11% systematic uncertainties on our data, and approximately $\pm$ 5% errors on the e-p data. We conclude that $\sigma(\mu p)$ and $\sigma(ep)$ are consistent to the accuracy of our measurements.

In each of these W bins we now look at the hadrons in the final state. Charged hadrons emerging from the vertex are highly visible, while neutrals are not seen unless they decay or interact before leaving the visible volume. Therefore, only charged hadrons contribute to the prong count. For example, a i-prong event has an outgoing negative μ (not counted) and a single positive particle. For elastic scattering, no other particles are involved in the final state. At higher W, a i-prong event always has one or more missing neutrals. A 3-prong event has two positive and one negative hadron, possibly some neutrals, and the (not counted) negative μ in the final state. Even-prong counts should not occur because of charge conservation. In our data, 4 events out of a total of 4700 had an even-prong count. These events can occur with small probability due to particles produced at rest, rescatter of outgoing particles near the vertex, of a small contamination of D_2 in the hydrogen of the bubble chamber.

In Figure 6a is see the break down of the cross section into its 1-prong and 3-prong fractional parts. No higher multiplicities occur in this W region. The cross section is predominantely 1-prong. The photoproduction values are shown on the left at $Q^2 = .0$. These points were obtained from Ref. 2.

In figure 6b is shown the range W = 1.8-2.8 GeV. Here the contribution to the total cross section includes 5-prong events. The 1-prong events show a contribution which lies significantly above the photoproduction value.
The 3-prong component is seen to decrease as Q^2 increases, and the small fraction of 5-prongs show no significant deviation from the photoproduction value. Here the photoproduction values come from data of Ref. 7.

In Figure 6c is the data for W = 2.8-3.8 GeV. Here too is seen the increasing 1-prong contribution to the total cross section as Q^2 increases, a corresponding 3-prong decrease and 5 and 7 prong components which are consistent with the photoproduction value (from Ref. 3). Figure 6d shows the corresponding data at W=3.8-4.8. At the highest W, evidence for the decreasing 3-prong contribution is no longer seen. The measured values are based on the data, and on the ratio to radiatively corrected e-p cross sections. To properly make the comparison, the electroproduction cross sections are averaged over the bins in Q^2 and W we have chose, and our cross sections are compared to these averaged values.

The data are corrected at all points for radiative processes from elastic scattering ("elastic tails") which is the dominant part of the radiative corrections in the kinematical range. Radiative corrections to the total cross section include corrections for inelastic scattering.

One may summarize the prong distribution information of Figures 6a-6d by computing $\langle N \rangle$, the mean charged hadronic prong multiplicity for inselected bins in Q^2 and W. To calculate this parameter, each event is weighted event by the inverse of the detection probability, in order to remove effects of the detection probability. For each selected bin in W, Q^2, is formed

$$\langle N \rangle = \frac{\sum_{\text{prongs}} n\sigma_n}{\sum_{\text{prongs}} \sigma_n} = \Big(\sum_{\text{all events}} N_i/P_i \Big) \Big/ \sum_{\text{all events}} 1/P_i$$

where N_i is the number of prongs in an event, and P_i is the muon detection probability derived from Monte Carlo calculations. We first study $\langle N \rangle$ as a function of Q^2 for fixed W ranges. The results are shown in Figure 7. We present results for three W intervals and three Q^2 intervals. Also shown are the photoproduction values at $Q^2 = 0$, obtained from data of Ref. 7. We observe that for the two lower W intervals, N decreases by 10% to 15% below the photoproduction values from $Q^2 = 0$ to Q^2=1.8 GeV^2. For the high W bin, a flat Q^2 dependence cannot be ruled out.

It was necessary to apply radiative corrections to these data. The influence of the "elastic tail" for example adds an excess of 1-prong events at higher W, causing the average multiplicity to be lowered. Tails from inelastic states also reduce the average multiplicity at high W. Careful study of this matter quantitatively shows that only the lowest Q^2 points at the highest W value are significantly altered. The calculation of the radiative corrections to the mean multiplicity are based on a model from electroproduction and photoproduction data which is discussed in ref. (1) in detail.

The multiplicity has also been studied as a function of Q^2 and W in the 2-4 GeV range for the photon framentation region ($x > +.3$), target fragmentation region ($x < -.3$), and the central region ($-.3 < x < +.3$). To do this we binned the charged hadrons from each event into their proper Q^2 and x regions, where $x = (P_\ell / P_{max})_{CMS}$. These results are shown in Figure 8. In the case in which the positive track identification was ambiguous, the pion hypothesis was selected, rather than the proton. Choosing the proton hypothesis for the track gives an x-value more positive than that for the pion because of the mass dependence of the Lorentz transformation to the C.M.S. Photoproduction data of Ref.3 were handled in the same way.

A recent measurement of multiplicities was made by a Cornell group and extended the kinematic range out to $Q^2(4\text{-}6)$ $(GeV/c)^2$. This experiment was done using a scintillation center recording the number of hits associated with a scattered electron. There results are shown in fig. 9 and show that in the Q^2 range greater than previously described $\langle n \rangle$ remains fairly constant with Q^2 at fixed W^2.

Charge Ratios for Hadrons

In the wide angle spectrometer experiment[4] a very interesting effect was observed when the hadron charge ratio was measured as functions of Q^2 for different values of the Feynman x. A typical set of data is shown in Fig. 10 for two values of x, one between x=0 and 0.3 and the other for $x > 0.3$. This result which has been confirmed by other experiments at lower Q^2 values is quite interesting because it lends itself to a quark-parton interpretation.
It is certainly difficult to explain in terms of the "dissociation" of the virtual photon.

These measurements were extended to deuterium in order to compare the effect for protons and neutrons.

The kinematic region of interest was limited to $-.25 > q^2 > -3.0$ GeV^2, and $12 < s < 30$ GeV^2. The no of events found were 30,401 electrons from H_2 and 14,772 from D_2. These electrons were divided into 16 bins in the q^2-s plane, and the number in each bin was taken to represent the total number of γ^*-p or γ^*-d interactions, effectively $\sigma_{tot}(q^2,s)$. These numbers were corrected bin-by-bin for geometric acceptance, scanning and measuring losses ($\sim$ 25%), radiative effects ($\sim$25%) and hadron contamination ($\sim$ 3%).

For the purpose of kinematic computations these events were all assumed to be π's. Events were selected having both an electron in the above q^2-s range, and a hadron in the range $0 < \varphi < 2\pi$, $p_\perp^2 < 0.7$ GeV^2 and $x > 0.1$. Of the inclusive hadronic events of this type there were 9250 from H_2 and 4663 from D_2. The losses in the number of electron-hadron events due to scanning and measuring inefficiency depend only slightly on hadron charge and on target type, and were typically $\sim$ 45%.

Cross sections were determined for reactions (1) and (2) by first fitting the hadron-electron events with a maximum-likelihood technique to the form

$$\frac{1}{\sigma_{Tot}(q^2,s)} \frac{d\sigma(q^2,s)}{dx\, dp_\perp^2\, d\varphi} = \frac{dN}{dx}\, b\, e^{-bp_\perp^2}\, \frac{(1 + A\cos\varphi + B\cos 2\varphi)}{2\pi} \tag{3}$$

The fitting function contained the normalization, $\sigma_{Tot}(q^2,s)$ determined from couting electrons, the detailed dependence of the geometric efficiency on the variables φ, $p_\perp^2$, x hadron charge, s and q^2, and the dependence of the scanning-measuring efficiency on hadron charge and target type. Fits were always done separately for H_2 and for D_2, for positive and negative hadrons, and for small intervals of x. The outputs of the fits included the differential multiplicities, dN/dx, the transverse momentum slope parameters, b, and the azimuthal asymmetries, A and B. The latter were always consistent with 0, and with 90% confidence never greater than 0.3. The following data described hereins are from fits in which A and B are fixed at 0.

The x-distributions for reaction (1) were reported earlier[4]. These distributions as well as those from D_2 are similar in shape to the distributions for inclusive π's in photoproduction[7], provided that decay π's from the reaction $\gamma p \to \rho^o p$ are removed. The $\rho^o p$ final state is known to be a smaller fraction of the total cross section as $|q^2|$ increases[1], however this effect is too small to account for the asymmetry to be discussed next.

Shown in Fig. 11a are the charge ratios for proton for $0.4 < x < 0.85$ and the same x range extracted from other experiments[1,8-11]. All of the other experiments have $\pi - K - p$ separation, and the results shown are explicitly the π^+/π^- ratios. We have concluded from the q^2 and s dependence of the inclusive k's and p's in one of these experiments[11] that the hadrons reported here are predominantly π's.

The neutron data this required a deuterium subtraction, to be discussed next. The principal assumption made was that the cross section for an inclusive process from deuterium,

$$\gamma^* d \rightarrow h^{\pm} + \text{anything} \tag{4}$$

is simply the sum of the corresponding cross sections for protons and neutrons. This assumption is justified by the observations that in this Q^2-s range (1) there is no evidence for "shadowing" in measurements of σ_{TOT} for heavy nuclei, (2) the deuterium "smearing" corrections to σ_{TOT} are negligible, and (3) no evidence was seen for coherent production from D_2 in the transverse momentum slopes.

Because the cross sections were in the form of differential multiplicities, internally normalized to the σ_{tot}'s, we subtracted them with the formula

$$\frac{dN}{dx_n} = \frac{\sigma_{tot}^{d}}{\sigma_{tot}^{n}} \frac{dN}{dx_d} - \frac{\sigma_{tot}^{p}}{\sigma_{tot}^{n}} \frac{dN}{dx_p} \tag{5}$$

The subtraction was done in separate x bins, and separate regions of the q^2-s plane. The ratios $\sigma_{tot}^{d}/\sigma_{tot}^{n}$ and $\sigma_{tot}^{p}/\sigma_{tot}^{n}$ depended on q^2 and s are were extracted from the literature[10]. Corrections were made for the target-empty events (4% of the D2 events), and for a 3% H_2 contamination in the D_2.

The charge ratio extracted for the neutron is shown in Fig. 11b. The errors shown represent statistical uncertainty only. There may be additional systematic errors no larger than $\pm$ 20% of the value of the charge ratio, due to uncertainty in the scanning and measuring efficiency. Included in Fig. 10 are charge ratios from photoproduction at s = 14.9.[8] There it has been noted that the following isospin symmetry holds for the π^+/π^- charge ratios:

$$\left(\frac{N^+}{N^-}\right)^p \approx \left(\frac{N^-}{N^+}\right)^n \approx 1.2 \tag{6}$$

In electroproduction we have found the charge ratios very much different.* First, we observe a striking hadron charge asymmetry from the p target, with $N^+/N^- \approx 2$ at $q^2 \approx -1$ GeV/c. Second, the isospin symmetry of Eq. (6) clearly breaks down, there appearing to be more h^+ than h^- from the n target also. These changes in the hadron composition occur in the kinematic region $0.4 < x < 0.85$, a region populated by the decay products or fragments of the γ^* in any diffractive model of γ^*-nucleon interactions. Since the γ^* is neutral, the charge asymmetries in electroproduction make any such diffractive model less attractive than in nearly-symmetric photoproduction. The above changes from the charge and isospin symmetric hadrons of photoproduction to the asymmetric hadrons of electroproduction take place in the q^2 range in which scaling begins.

We wish to point out that the behavior shown in Fig. 10 has a natural explanation in a quark-par ton model. In such a model the γ^* strikes p-type (charge $+\frac{2}{3}$) valence quarks in preference to n-type (charge $-\frac{1}{3}$) valence quarks. These struck quarks fragment in the fragmentation region, the p-type preferentially to π^+, the n-type preferentially to π^-. This gives a net π^+ excess for the proton, and a smaller π^+ excess for the neutron. This model gives a testable prediction[12] for the pion multiplicities in our x range:

$$R = \frac{\int_1^\infty (N_n^+ - N_n^-)\, F_1^n(\omega)\, \frac{d\omega}{\omega^2}}{\int_1^\infty (N_p^+ - N_p^-)\, F_1^p(\omega)\, \frac{d\omega}{\omega^2}} = \frac{2}{7} = 0.29 \tag{7}$$

Here ω is the scaling variable, $\omega = (q^2+M^2-s)/q^2$, $F_1(\omega)$ is a known inelastic structure function, and p and n represent the proton and neutron. We are able to test this prediction with our data only over the limited range $3 < \omega < 60$, and here compute the value $R = .24 \pm .28$. Clearly a more precise test of relation (7) is needed. A more detailed discussion of these results in relation to be quark--parton model is reported separately[5].

Vector Meson Electroproduction.

All there vector mesons, ρ^o, ω and φ have been seen in electroproduction. There is no evidens yet for ρ', that only because of two poor events. Mostly the a detailed information concern the ρ^o

Figure 12 shows the $\pi^+\pi^-$ invariant mass distribution for the three Q^2 intervals with $W > 2$ GeV. A strong rho signal is seen in all Q^2 intervals. In addition, some $\Delta^{++}(1236)$ production is observed.

A similar plot is shown in Fig. 13, for the wide angle spectrometer.

In Fig. 14 is given the relative contribution of reaction 3 to the total cross section along with the photoproduction[(7)] result averaged over the W dependence of this experiment. The contribution decreases from 22% to about 12% when going from $Q^2 = 0$ to $Q^2 = 1\ GeV^2$. In Fig. 14 the contribution of Δ^{++} and ρ^o production to the total cross section are displayed. The relative importance of ρ^o production decreases with Q^2 by about a factor of 2 over our Q^2 range.

In photoproduction, the t-distribution for $|t| < 0.6\ GeV^2$ can be fit well by a form exp (A t) where the slope A is found to be 7 to 8 GeV^{-2} for photon energies above 2 GeV (using the parameterization procedure discussed above to describe the ρ mass shape).[(2)]

To compare our data to photoproduction we have fit the Dalutz plot density as before with a factor exp (A t) multiplying the ρ contribution. Only events with $|t| < 0.6\ GeV^2$ were used in the fit. The slope parameter A as determined in the fit is given in Fig. 15. It shows a small decrease of $\sim 20\%$ by $Q^2 = 1\ GeV^2$, but is also consistent with no decrease with Q^2.

Fig. 16 shows the slope data for the wide angle spectrometer experiment which shows the same general effects. Taking both experiments together one might conclude that some evidence for anti-shrinkage is beginning to appear for $Q^2 > 1$.

For the description of the ρ^o decay when produced in the inelastic scattering, the usual density matrix representation[11] must be expanded to include production by longitudinal photons. We use the definition of Ref. 11b. If ϑ and φ are the polar and azimuthal angles of the π^+ in the ρ^o rest system (with the z axis along the CMS ρ^o direction, the x axis in the hadron production plane, and Φ the azimuth of the scattered μ^- with repsect to the hadron production plane in the hadronic CMS), then the angular distribution of ρ decay is:

$$W(\cos\theta,\phi,\Phi)=\frac{3}{4\pi}\Big[\frac{1}{2}(1-r^{04}_{00})+\frac{1}{2}(3r^{04}_{00}-1)\cos^2\theta-\sqrt{2}\,\mathrm{Re}\,r^{04}_{10}\sin2\theta\cos\phi-r^{04}_{1-1}\sin^2\theta\cos2\phi$$
$$-\epsilon\cos2\Phi\{r^1_{11}\sin^2\theta+r^1_{00}\cos^2\theta-\sqrt{2}\,\mathrm{Re}\,r^1_{10}\sin2\theta\cos\phi-r^1_{1-1}\sin^2\theta\cos2\phi\}$$
$$-\epsilon\sin2\Phi\{\sqrt{2}\,\mathrm{Im}\,r^2_{10}\sin2\theta\sin\phi+\mathrm{Im}\,r^2_{1-1}\sin^2\theta\sin2\phi\}$$
$$+\sqrt{2\epsilon(1+\epsilon+\Delta)}\cos\Phi\{r^5_{11}\sin^2\theta+r^5_{00}\cos^2\theta-\sqrt{2}\,\mathrm{Re}\,r^5_{10}\sin2\theta\cos\phi-r^5_{1-1}\sin^2\theta\cos2\phi\}$$
$$+\sqrt{2\epsilon(1+\epsilon+\Delta)}\sin\Phi\{\sqrt{2}\,\mathrm{Im}\,r^6_{10}\sin2\theta\sin\phi+\mathrm{Im}\,r^6_{1-1}\sin^2\theta\sin2\phi\}\Big]$$

where the polarization parameter

$$\varepsilon=\frac{1}{1+\dfrac{2(Q^2+\nu^2)\tan^2\Theta/2}{Q^2\,(1-Q^2_{Min}/Q^2)^2}}$$

and $Q^2_{min}=2\,(EE'-|\vec{p}|\,|\vec{p}'|\;-M^2)$, $\nu=E-E'$, and Θ is the muon polar scattering angle. The density matrix elements r^{α}_{ii} are the same as for polarized photons except

$$r^{o4}_{\lambda k}=\frac{\rho^{oT}_{ik}+(\epsilon+\mathring{\Delta})R\,\rho^{oS}_{ik}}{1+(\epsilon+\Delta)R}\;,\qquad r^{\alpha}_{ik}\quad \alpha=1,2\quad \frac{\rho^{\alpha}_{ik}}{1+(\epsilon+\Delta)R}$$

where T and S refer to production by transverse and longitudinal photons respectively and Δ is defined as $\Delta=\dfrac{2M^2_{\mu}(1-\varepsilon)}{Q^2}<<1$. It is clear that ρ^{oT} and ρ^{oS} can only be separated by varying $\varepsilon+\Delta$ at fixed W and Q^2; for our data no separation is possible because we had a fixed incident muon energy.

In Fig. 17 we show the angular distribution in $\cos\vartheta$ and $\psi=\varphi-\Phi$ of ρ^o decay for $Q^2>0.15$ GeV^2 and $W>2$ GeV. Cuts to define the ρ^o are $0.6<M_{\pi\pi}<0.9$ GeV and $|t|<0.6$ GeV^2. The data are consistent with isotropy in $\cos\vartheta$.

If s-channel helicity conservation (SCHC), found in ρ^o-photoproduction, is valid for leptoproduction, the $\sin^2\vartheta$ part of this distribution comes entirely from transversely polarized virtual photons while the $\cos^2\vartheta$ component measures that from longitudinal photons. Assuming SCHC, the ratio of longitudinal to transverse ρ production cross section is

$$R=\frac{\sigma_L(\rho)}{\sigma_T(\rho)}=\frac{1}{<\epsilon>}\quad\frac{r^{04}_{00}}{1-r^{04}_{00}}$$

The azimuthal distribution shown in Fig. 17 peaks at 0° and 180°, indicating dominant t-channel natural parity exchange for the transverse beam component, as is found in photoproduction. In the scatter plot of the same figure, the effect of interference between longitudinal and transverse ρ^0 can be seen as enhanced $\psi = 0°$ (360°) production for $\cos\vartheta < 0$, and enhanced $\psi = 180°$ production for $\cos\theta > 0$. A measure of this interference is given by

$$\cos\delta = \sqrt{\frac{2 < \epsilon >}{r^{04}_{00}\,(1-r^{04}_{00})}}\left(\mathrm{Re}\ r^5_{10} - \mathrm{Im}\ r^6_{10}\right)$$

and $\cos\delta = 1$ indicates maximum interference.

From the ρ^0 decay angular distribution the values for the density matrix of Eq. 4 were determined from a moment analysis for events in the ρ^0 mass region. For this analysis we used events with $W > 2.5$ GeV and $Q^2 > 0.2$ GeV^2, in order to eliminate background from the final state $\pi^-\Delta^{++}$. We estimate that only $\approx 2\ \Delta^{++}$ are left using these cuts. The values for all parameters are given in Table II.

If s-channel helicity is conserved we expect all density matrix elements to be zero except r^{04}_{00}, r^1_{1-1}, $\mathrm{Im}\,r^2_{1-1}$, $\mathrm{Re}\,r^5_{10}$, $\mathrm{Im}\,r^6_{10}$. Within one to two standar deviations the density matrix elements of Table II are consistent with SCHC with the exception of r^1_{00} which shows a 2-3 standard deviation effect from 0. If confirmed $r^1_{00} > 0$ would imply a contribution from single flip helicity amplitudes. However, if we assume that the ρ^0 production mechanism conserves SCHC for $Q^2 > 0$, then r^{04} measures $R = \frac{\sigma_L(\rho)}{\sigma_T(\rho)} = \frac{1}{\langle\varepsilon\rangle}\frac{r^{04}_{00}}{1-r^{04}_{00}} = 0.54 \pm 0.23$; the ratio of the longitudinal to transverse ρ production. A measure of the interference between these amplitudes which is seen in the decay distribution of Fig. 17 is

$$\cos\delta = 0.76 \pm 0.17.$$

For the data with $Q^2 > 0.2$ GeV^2 and $W > 2.5$ GeV the average value of ε is 0.89.

If we assume SCHC holds in electroproduction, as it approximately does in photoproduction, the decay angular distribution reduces to

$$W(\theta,\psi) = \frac{3}{8\pi^2(1+\epsilon R)}\left[\epsilon R\cos^2\theta + \frac{1}{2}\sin^2\theta(1+\epsilon\cos 2\psi) - (\epsilon R(1+\epsilon)/2)^{\frac{1}{2}}\cos\delta\sin 2\theta\cos\psi\right] \tag{5}$$

We can then determine the two free parameters, R and $\cos\delta$ for finer Q^2 intervals than above by a maximum likelihood fit to the events of reaction (3) with $W > 2$ GeV; accounting for the $\Delta^{++}\pi^-$ and phase space contributions as explained in the discussion of cross section determinations. While only events with $|t| < 0.6$ GeV were used in the fit, the parameter R and cos did not change when all events were used. In Fig. 18 and give R and $\cos\delta$ from these fits along with the data of Dakin et al.[4] in the indicated Q^2 intervals. Within errors the experiments agree and show a large contribution of longitudinally polarized rhos which interfere maximally with the transverse component.

In Fig. 19a is plotted the $\pi^+\pi^-\pi^0$ mass distribution from the reaction $\mu^-p \to \mu^-p\,\pi^+\pi^-\pi^0$. The events shown have a 1C fit confidence level greater than 3%, $Q^2 > 0.2$ GeV^2 and $W > 2.0$ GeV. A clear

ω peak is seen. The shaded events have $Q^2 > 0.5$ GeV^2 and also show a strong ω peak. While the events plotted have not been weighted by our acceptance, such weighting makes little change in the observed structure. We have estimated the ω cross section by selecting events with $0.74 < M(3\pi) < 0.82$ GeV, making a small background correction by hand, and correcting for our 3% probability cut and non 3 π decay modes. In Fig. 19b we plot the ratio $\sigma(\gamma_v p \to p\omega)/\sigma_{Tot}$ vs Q^2 for $W > 2.0$ GeV. Using photoproduction data(7) we have calculated the ratio $\sigma(\omega)/\sigma_{Tot}$ at $Q^2=0$ for the same W interval (correcting for the photon energy spectrum). Our data points agree well with the photoproduction value, but do not exclude the Q^2 variation found for $\sigma(\rho)/\sigma_{Tot}$. Since the ω can be produced by both OPE and diffraction scattering our previous observation of a decrease in the ρ^o contribution to the total cross section at larger Q^2 need not imply a similar decrease in $\sigma(\omega)/\sigma_{Tot}$.

For the ω events with $|t| < 0.5$ (GeV/c)^2 we find an exponential slope (e^{At}) of $A = 7.5 \pm 1.5$ GeV^{-2}. The ω angular distributions in the helicity frame, cos θ_H and ψ_H are consistent with isotropy and are similar to the angular distributions above the ω peak. We find $r^{04}_{oo} = 0.20 \pm 0.15$ for ω events with $Q^2 > 0.2$ GeV^2. This result is consistent with the photoproduction data(7). We find no evidence for 3-body resonance production other than the ω in the $\pi^+\pi^-\pi^o$ final state. In the 2-body channels we find a strong $\Delta^{++}(1238)$ signal and some weak evidence for Δ^+ and ρ^o production. φ electroproduction has been observed in wide angle spectrometer experiment. Figure 20 shows the dikaon mass distribution for events consistent with the hypothesis

$$\gamma^* p \to K^+ K^- p$$

There are six events at the mass of the φ meson. We estimate that the background from electron, muon, and pion pairs is 1 ± 1 event. The average q^2 of the events is $-.6$ (GeV/c)^2 and the average s is 22.9 GeV^2. The acceptance for φ's was 60% larger than that for ρ^o's; the corrections were similar except for meson mass cut, K decay, and unseen decay modes.

The ratio of the φ virtual photoproduction cross section to the total virtual photoproduction cross section is $.0017 \pm .0009$ compared to $.0046 \pm .0006$ for photoproduction(7).

REFERENCES

(1) - Ballam, Bloom, Carroll, Chadwick, Coltrell, Della Negra, De Staebler, Gershwin, Keller, Mestoyer, Moffeit, Prescott, Stein. Submitted to the Bonn Symposium on Electron and Photon Interaction, (1973) (total cross-section and multiplicities).

(2) - Same as (1) above (Vector Meson Electroproduction).

(3) - Same as (1) above (Inclusive Reactions).

(4) - Dakin, Feldman, Lakin, Martin, Perl, Petrasche, Toner, Phys. Rev. Lett. 30, 142 (1973) and SLAC-PUB-1211 (March 1973) Subm. to Phys. Rev. D.

(5) - Dakin, Feldman, Martin, Perl and Toner, SLAC-PUB-1269, July 1973, Subm. to Phys. Rev. Lett.

(6) - Dakin, J.T. and Feldman G.J. SLAC-PUB-1273, July 1973, Subm. to Phys. Rev. D.

(7) - SLAC-LBL-TUFTS Collab. J. Ballam et al. Phys. Rev. D5, 545 (1972);
K.C. Moffeit et al. Phys. Rev. D5, 1603 (1972)

(8) - J. Gandsman et al. Phys. Dept. Tel-Aviv Univ. Report TAUP-360-73.

(9) - F. Dammann et al., Nucl. Phys. B54, 381 (1973).

(10)- J.C. Adler et al. Nucl. Phys. B46, 415 (1972).

(11)- C.J. Bebele et al., Phys. Rev. Lett. 30, 624 (1973).

(12)- Cronon, Ravndal and Zarmi, Nucl. Phys. B51, 611 (1973).

(13)- Berkelman, Carbin , Gibbard, Wanderer - Cornell Report CLNS-240 Aug. 1973.

(14)- Bulos, Busza, Grise, Kluge, Larsen, Leith, Williams XVI High Energy Conference, Batavia I11. September 1972.

(15)- K. Schilling and G. Wolf - DESY Report 73/13 1973.

(16)- V. Echardt et al. - Nucl. Phys. B55 45 (1973).

FIGURE CAPTIONS

1. - a) Diagram of the scattering process with the variables Q^2 and W defined.

   b) Domain in the variable Q^2 of electroproduction, photoproduction and colliding beams experiments.

2. - Schematic representation of the experiment from the origin of the muon beam to the muon telescope hebind the 40-inch hydrogen bubble chamber. The upper part of the figure, depicting the muon beam, is not to scale.

3. - a) Distribution of data in Q^2 and W. Elastic scattering occurs at the left. Some resonance production is evident. The accumulation of events at high W low Q^2 is due to the shape of our acceptance function combined with the large cross section at small Q^2. Contours displayed are the acceptance probability for the μ-detector. These are calculated by a Monte Carlo program. The value of the acceptance is independent of the hadronic final state, since only the μ is required in the trigger.

   b) Same data as 3a). Contours of ε the polarization parameter, Eq. 9, and ω' the scaling variable, are shown.

4. - Schematic representation of the wide angle spectrometer experiment, showing the super conducting tube location.

5. - Detection efficiency contours for the WAS.

6. - a) Inelastic cross sections and prong contributions.

   W = 1.4 - 1.8 GeV

   The rapiditively corrected inelastic cross sections $\sigma_t + \epsilon\sigma_S$ are compared to radiatively corrected e-p cross sections. Also shown are the fraction of the total cross section which fall into 1 charged hadron (1-prong) and 3 charged hadron final states, for increasing Q^2. Contributions from radiative effects of elastic scattering ("elastic tails") are subtracted. Photoproduction points were obtained from Ref. 2.

   b) Inelastic cross sections and prong contributions.

   W = 1.8 - 2.8

   c) Inelastic cross sections and prong contributions.

   W = 2.8 - 3.8

   d) Inelastic cross sections and prong contributions.

   W = 3.8 - 4.8

7. - Average charged hadron multiplicity.

   We show three regions in W, with increasing Q^2 in each. The photoproduction values are obtained from Ref. 3, with small adjustments so that they coincide in $\langle W \rangle$, the mean value for the bins. The values shown are radiatively corrected according to the procedure discussed in the text.

8. - Average charged hadron multiplicity in the inclusive spectra.

   We present average charged hadron multiplicities for the target fragmentation, central plateau, and photon fragmentation regions, as Q^2 increases. Photoproduction data were obtained from Ref.3. The horizontal bands accompanying the photoproduction points indicate the variation in the photoproduction value for the different $\langle W \rangle$ values associated with our data in each bin. No radiative corrections were applied to these points because of lack of a good model.

9. - Average multiplicities plotted as a function of Q^2 for several ranges of s. For comparison we have also plotted data of ref. 16 (triangles), ref. 2 (open circles), and ref. 7 (crosses).

10.- The ratio +/- plotted versus Q^2 for two differmnt x ranges.

11.- a,b. Comparison of proton and neutron data for the charge ratio at large positive x values.

12.- Reaction $\gamma_v p \rightarrow \pi^+\pi^- p$, $\pi^+\pi^-$ mass distributions for different Q^2-intervals, Hybrid Data

13.- $\pi^+\pi^-$ mass distribution for WAS data - all Q^2.

14.- ratio of $\gamma_v p \rightarrow \pi^+\pi^- p / \gamma_v p \rightarrow$ hadrons top

   ratio of $\gamma_v p \rightarrow \pi^-\Delta^{++} / \gamma_v p \rightarrow$ hadrons middle

   ratio of $\gamma_v p \rightarrow \rho^o p / \gamma_v p \rightarrow$ hadrons bottom

   Photoproduction value from data of SBT collaboration (Ref. 3).

15.- Q^2-dependence of the exponential slope A for the reaction $\gamma_v p \rightarrow \rho^o p$ with $|t_{\rho\rho}| < 0.6\ GeV^2$ for the Hybind Data

16.- Same as Fig. 15, but for the WAS data.

17.- Reaction $\gamma_V p \to \rho^0 p$ for $Q^2 > 0.15$ GeV^2 and $W > 2.0$ GeV: Decay angular distribution of events in the ρ^0 region in the helicity system.

18.- Reaction $\gamma_V p \to \rho^0 p$ for $W > 2.0$ GeV: The ratio of longitudinal to transverse ρ^0 production and cosine of the longitudinal - transverse phase difference assuming s-channel helicity conservation.

19.- Reaction $\gamma_V p \to \pi^+\pi^-\pi^0 p$: a) $\pi^+\pi^-\pi^0$ mass distributions. b) $\sigma(\gamma_V p \to \omega p)/\sigma_{tot}$

20.- K^+K^- Mass distribution - showing a φ peak.

21.- Reaction $\gamma_V p \to \pi^-$ + (anything): Normalized structure function F(x) versus x for the indicated Q^2 and W intervals. The dashed curves are approximations to the photoproduction data of Ref. 3.

22.- Reaction $\gamma_V p \to \pi^-$ + (anything): Normalized structure function F(x) versus x for the indicated W and Q^2 intervals. Some proton contamination occurs for $x > 0$ for $W < 2.5$ GeV and $x > -0.5$ for $W > 2.5$ GeV. The dashed curves give the behavior at $Q^2 = 0$ of the photoproduction data of Ref. 3 and 5.

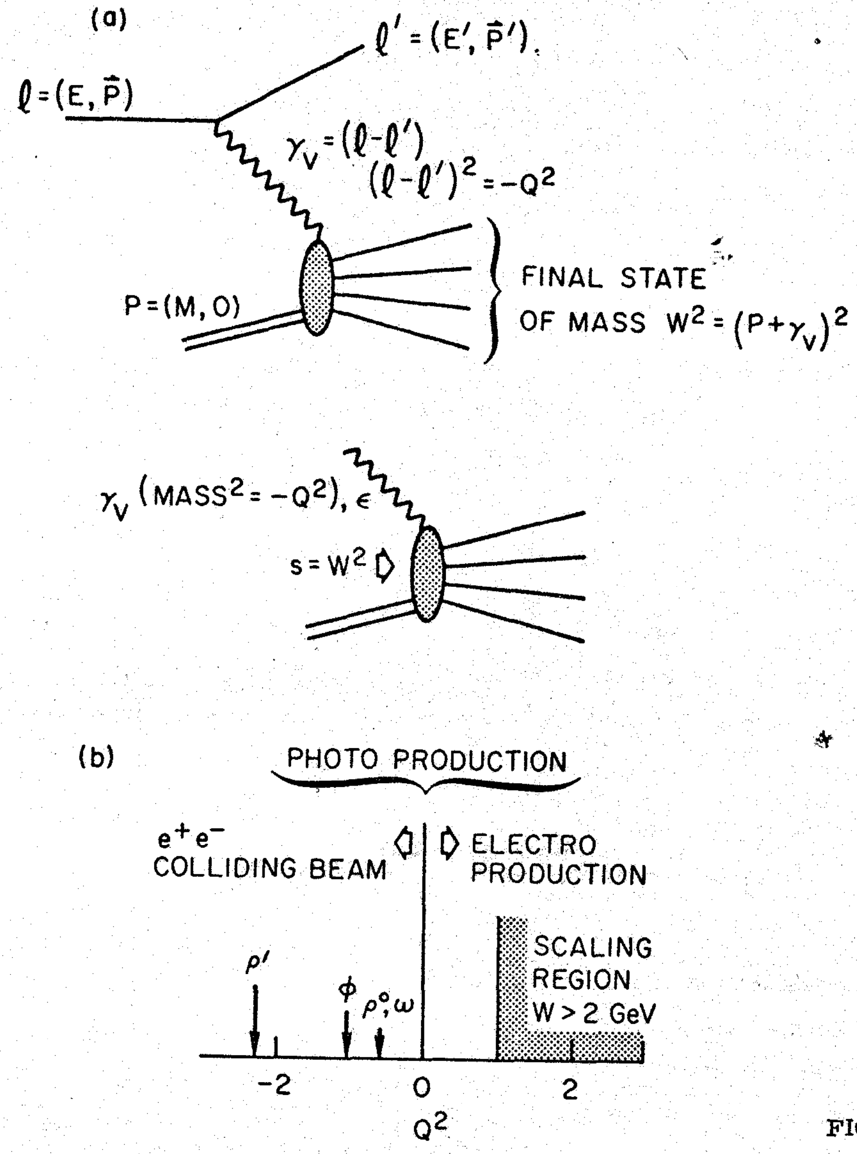

FIG. 1

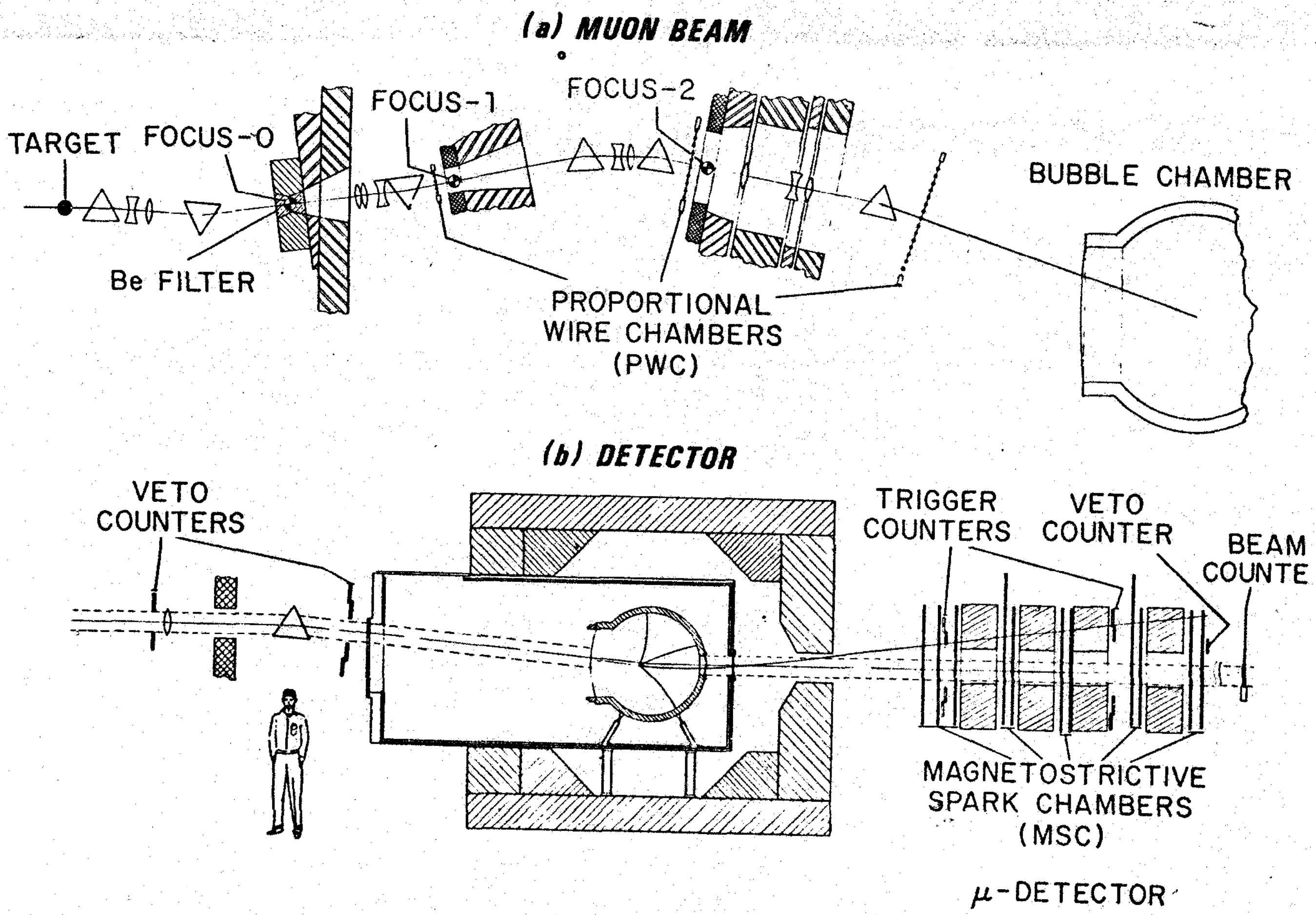

FIG. 2

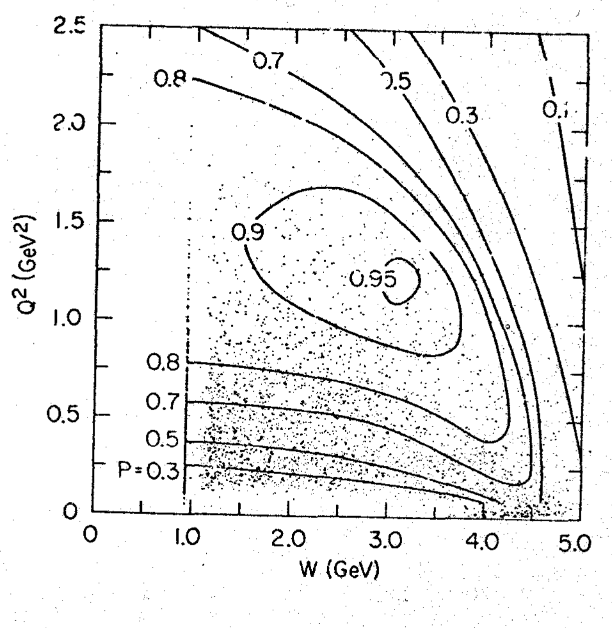

FIG. 3 a

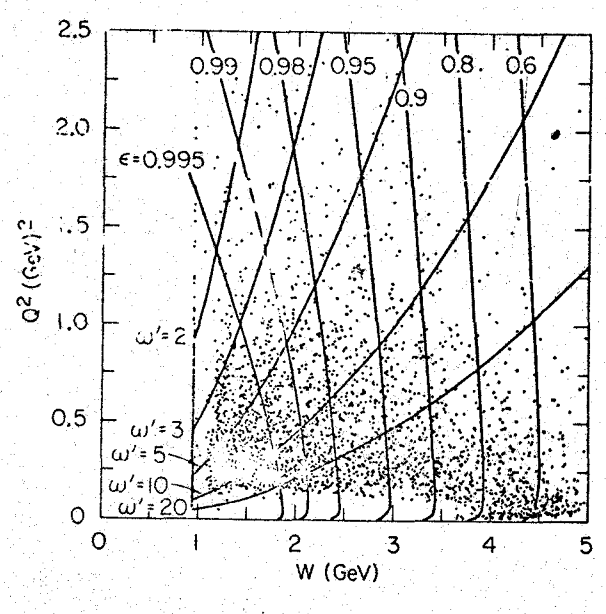

FIG. 3 b

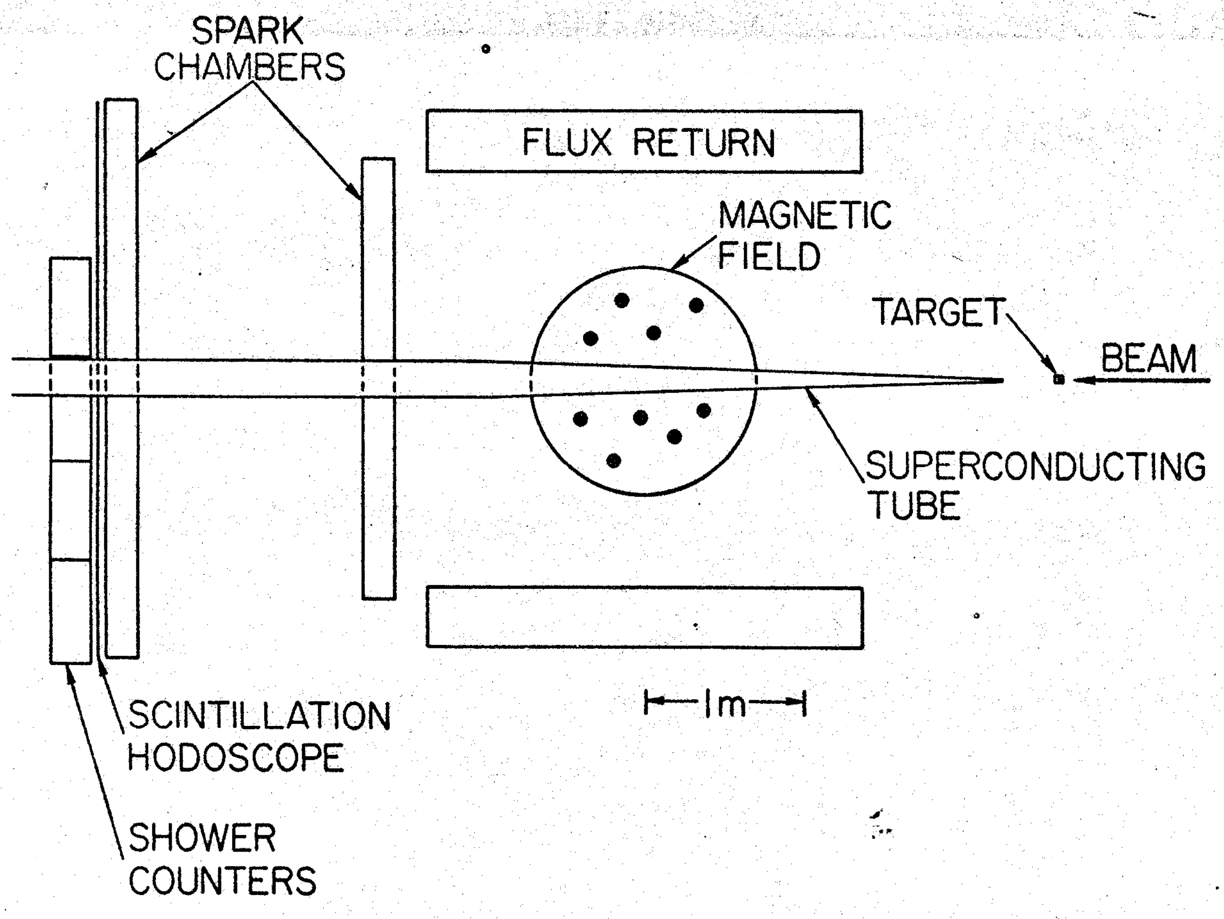
SPARK
CHAMBERS
FLUX RETURN
MAGNETIC
FIELD
TARGET
BEAM
SUPERCONDUCTING
TUBE
SCINTILLATION
HODOSCOPE
SHOWER
COUNTERS
1m

FIG. 4

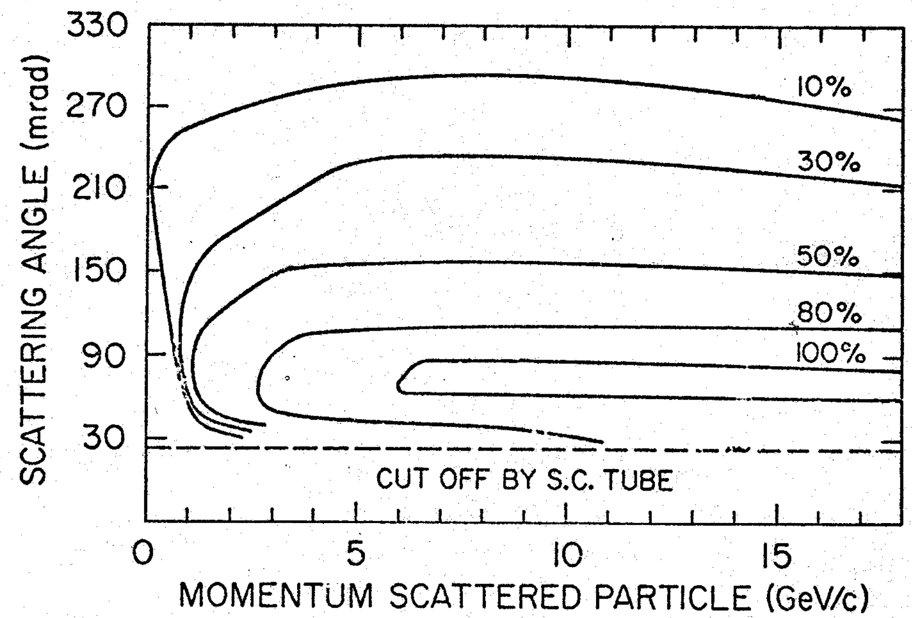
SCATTERING ANGLE (mrad)
330
270
210
150
90
30
10%
30%
50%
80%
100%
CUT OFF BY S.C. TUBE
0
5
10
15
MOMENTUM SCATTERED PARTICLE (GeV/c)

FIG. 5

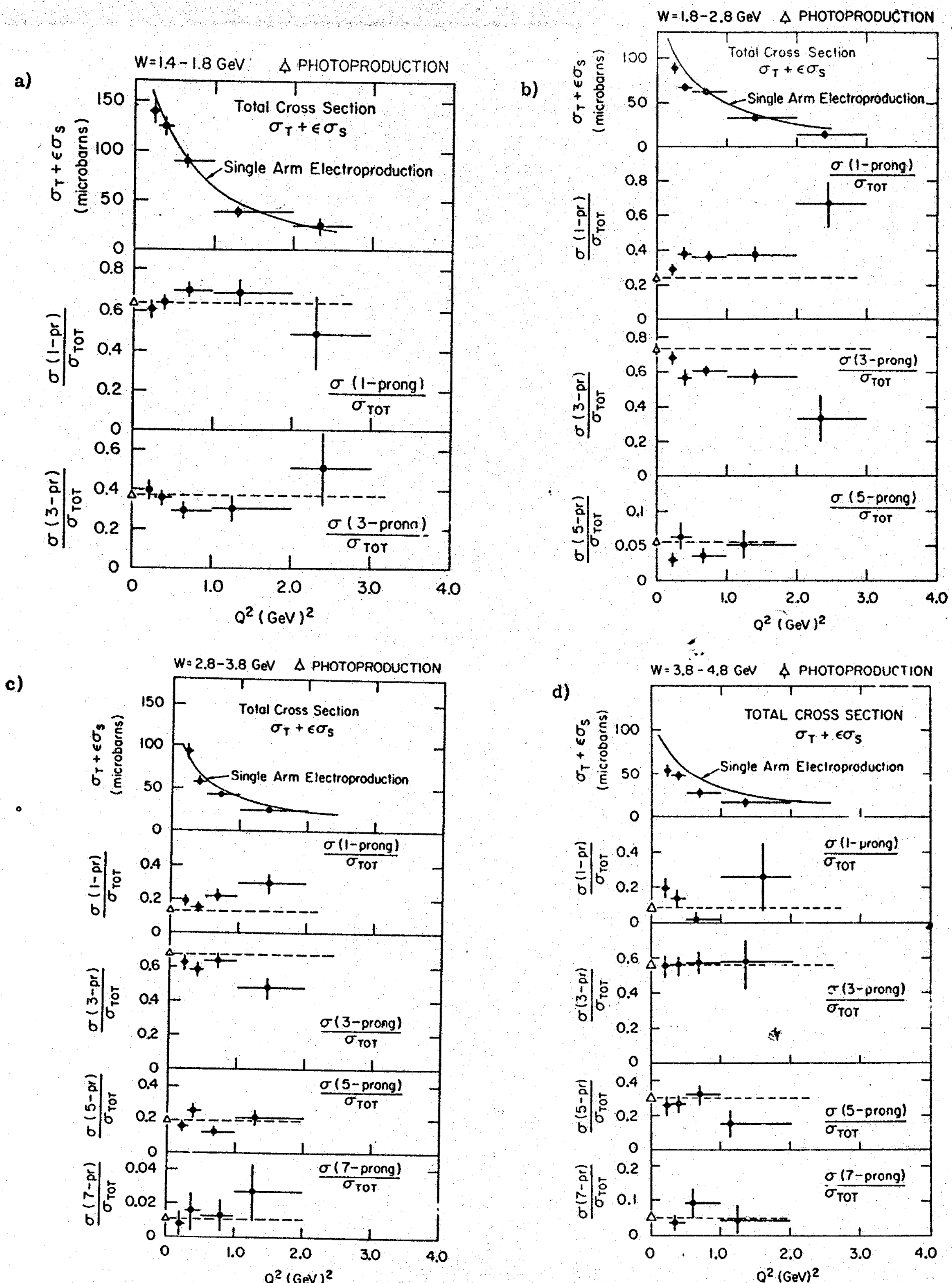
a)
W=1.4 - 1.8 GeV
PHOTOPRODUCTION
Total Cross Section
$\sigma_T + \epsilon\sigma_S$
Single Arm Electroproduction
$\sigma_T + \epsilon\sigma_S$ (microbarns)
$\frac{\sigma\ (1\text{-pr})}{\sigma_{TOT}}$
$\frac{\sigma\ (1\text{-prong})}{\sigma_{TOT}}$
$\frac{\sigma\ (3\text{-pr})}{\sigma_{TOT}}$
$\frac{\sigma\ (3\text{-prong})}{\sigma_{TOT}}$
Q^2 (GeV)^2
b)
W=1.8-2.8 GeV
PHOTOPRODUCTION
Total Cross Section
$\sigma_T + \epsilon\sigma_S$
Single Arm Electroproduction
$\frac{\sigma\ (5\text{-prong})}{\sigma_{TOT}}$
c)
W=2.8-3.8 GeV
$\frac{\sigma\ (7\text{-prong})}{\sigma_{TOT}}$
d)
W=3.8-4.8 GeV
TOTAL CROSS SECTION

FIG. 6

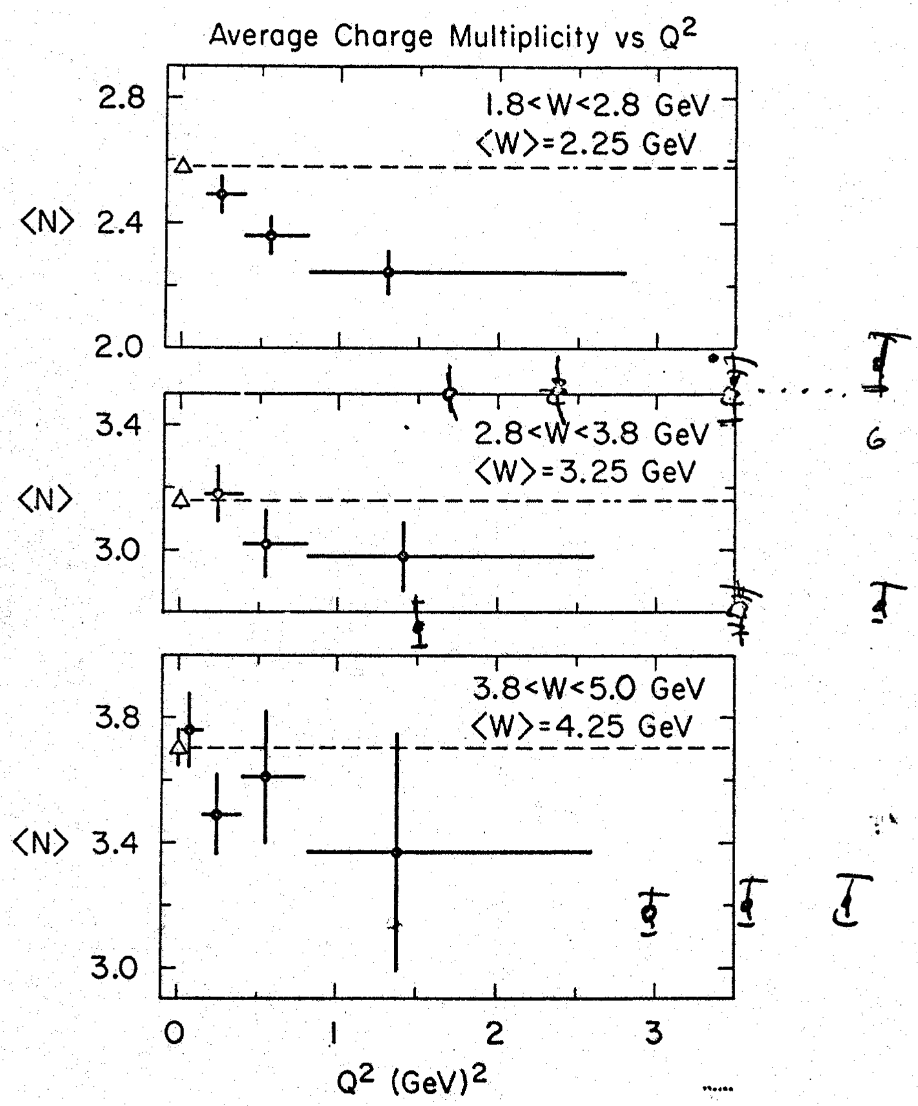

Average Charge Multiplicity vs Q^2
1.8<W<2.8 GeV
⟨W⟩=2.25 GeV
2.8<W<3.8 GeV
⟨W⟩=3.25 GeV
3.8<W<5.0 GeV
⟨W⟩=4.25 GeV
⟨N⟩
2.8
2.4
2.0
3.4
3.0
3.8
3.4
3.0
0
1
2
3
Q^2 (GeV)^2

FIG. 7

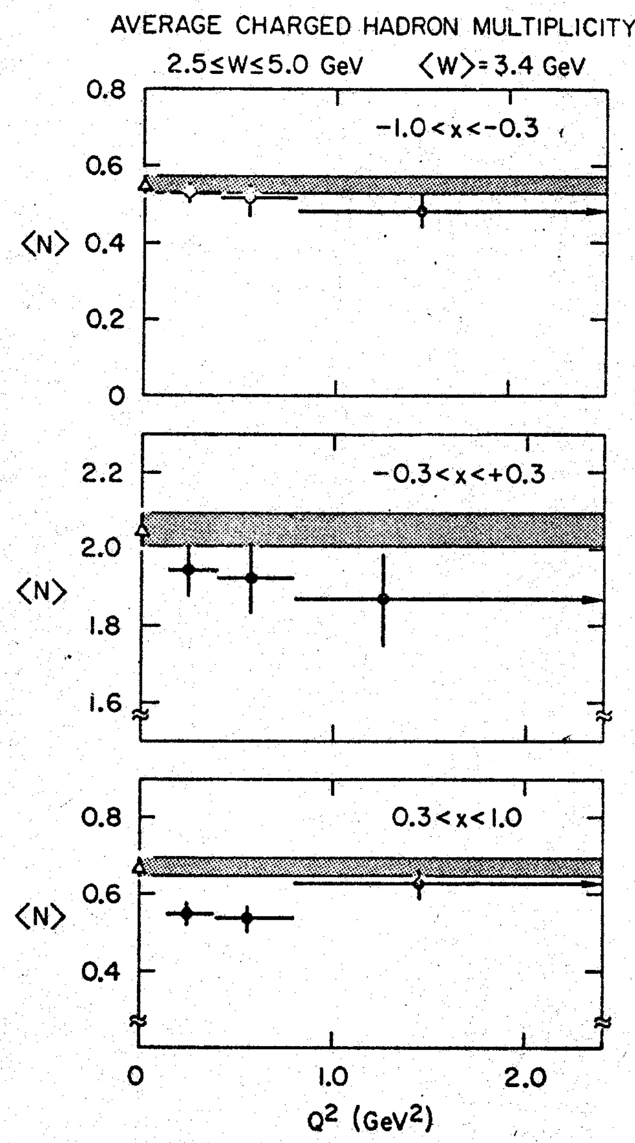

AVERAGE CHARGED HADRON MULTIPLICITY
2.5≤W≤5.0 GeV ⟨W⟩=3.4 GeV
−1.0<x<−0.3
−0.3<x<+0.3
0.3<x<1.0
⟨N⟩
0.8
0.6
0.4
0.2
0
2.2
2.0
1.8
1.6
0.8
0.6
0.4
0
1.0
2.0
Q^2 (GeV^2)

FIG. 8

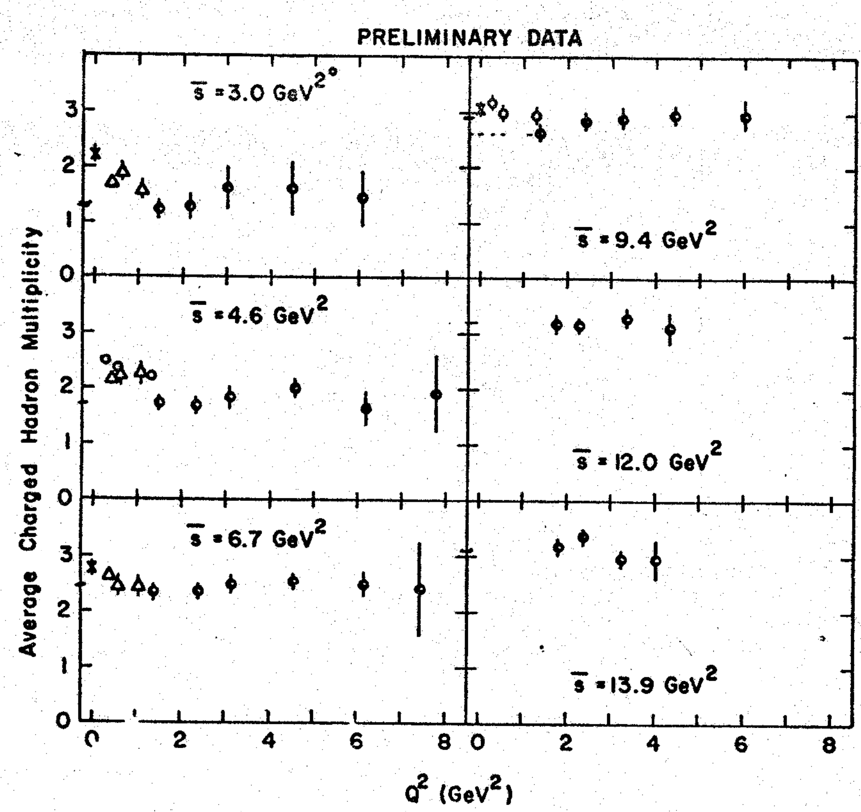
PRELIMINARY DATA
$\bar{s}$ = 3.0 GeV^2
$\bar{s}$ = 9.4 GeV^2
$\bar{s}$ = 4.6 GeV^2
$\bar{s}$ = 12.0 GeV^2
$\bar{s}$ = 6.7 GeV^2
$\bar{s}$ = 13.9 GeV^2
Average Charged Hadron Multiplicity
Q^2 (GeV^2)

FIG. 9

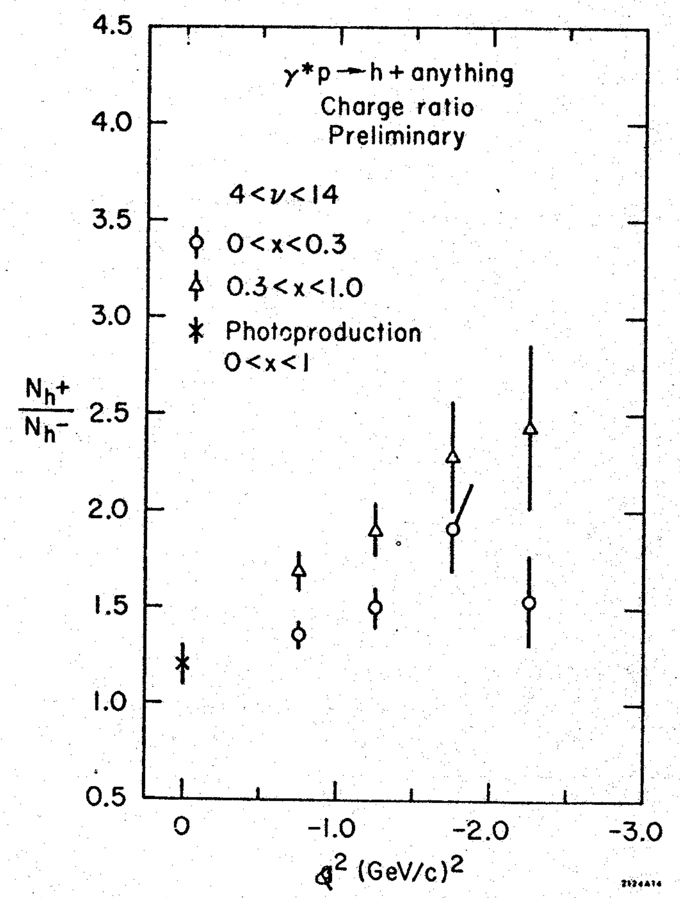
$\gamma^* p \to h$ + anything
Charge ratio
Preliminary
$4<\nu<14$
$0<x<0.3$
$0.3<x<1.0$
Photoproduction
$0<x<1$
$\frac{N_{h^+}}{N_{h^-}}$
q^2 (GeV/c)^2

FIG. 10

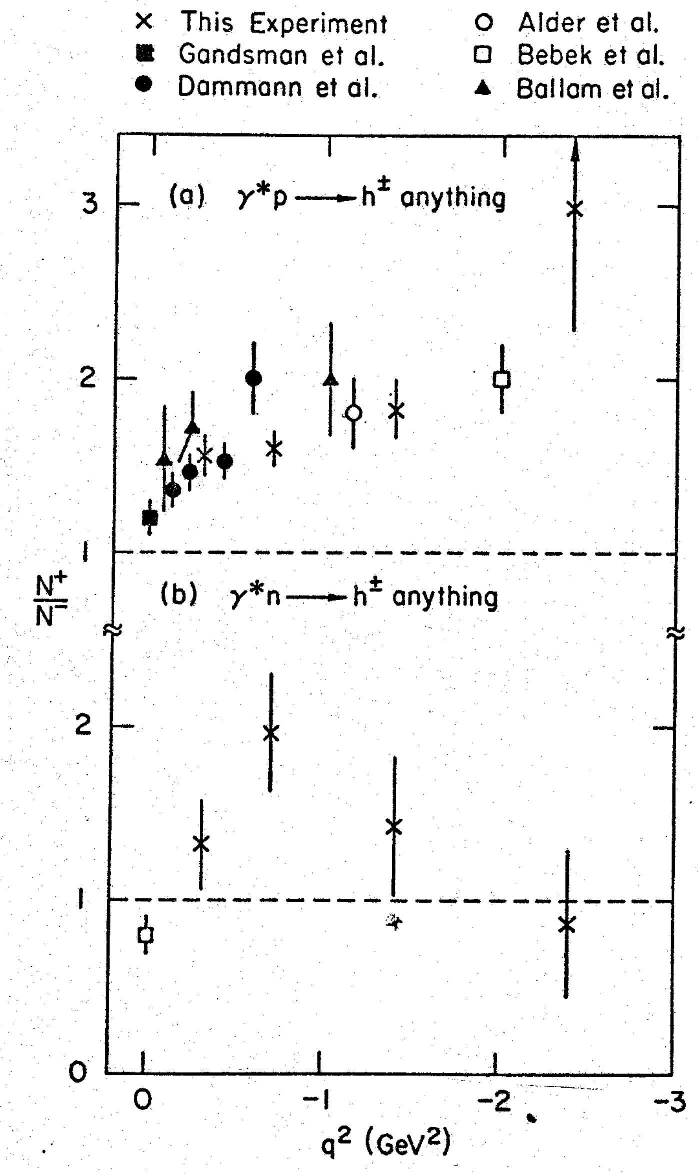
× This Experiment
Gandsman et al.
Dammann et al.
Alder et al.
Bebek et al.
Ballam et al.
(a) $\gamma^* p \longrightarrow h^{\pm}$ anything
(b) $\gamma^* n \longrightarrow h^{\pm}$ anything
$\frac{N^+}{N^-}$
q^2 (GeV^2)

FIG. 11

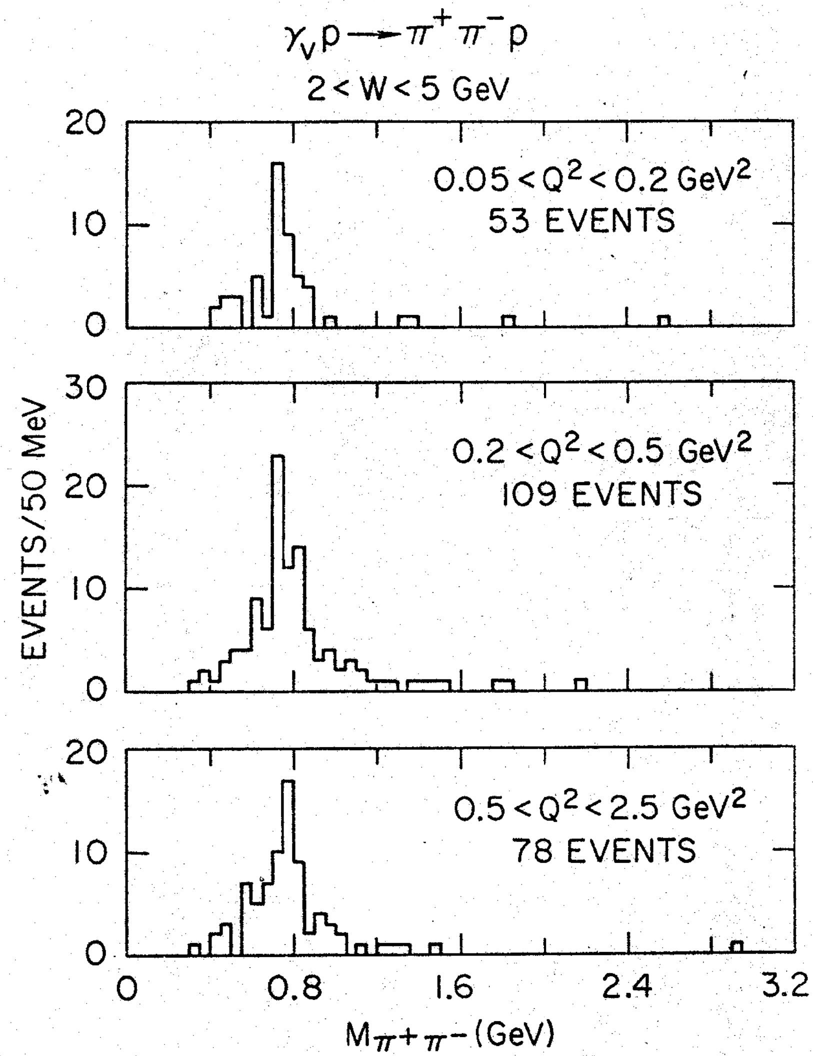
$\gamma_V p \longrightarrow \pi^+ \pi^- p$
$2 < W < 5$ GeV
$0.05 < Q^2 < 0.2$ GeV^2
53 EVENTS
$0.2 < Q^2 < 0.5$ GeV^2
109 EVENTS
$0.5 < Q^2 < 2.5$ GeV^2
78 EVENTS
EVENTS/50 MeV
$M_{\pi^+\pi^-}$ (GeV)

FIG. 12

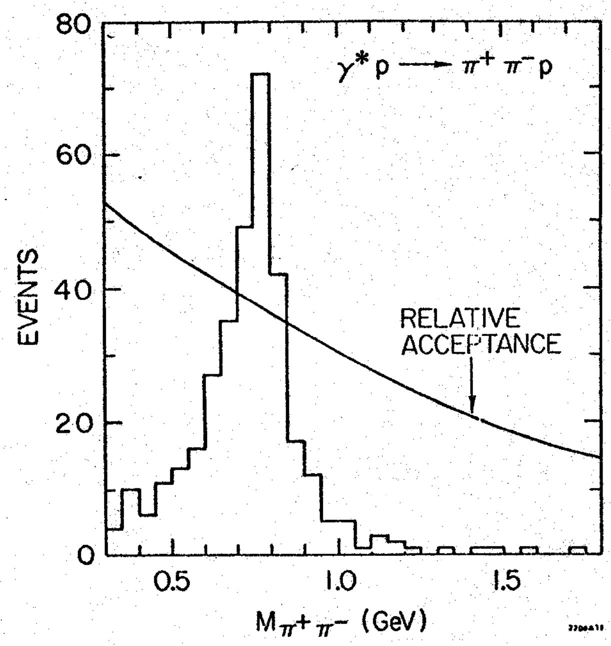

FIG. 13

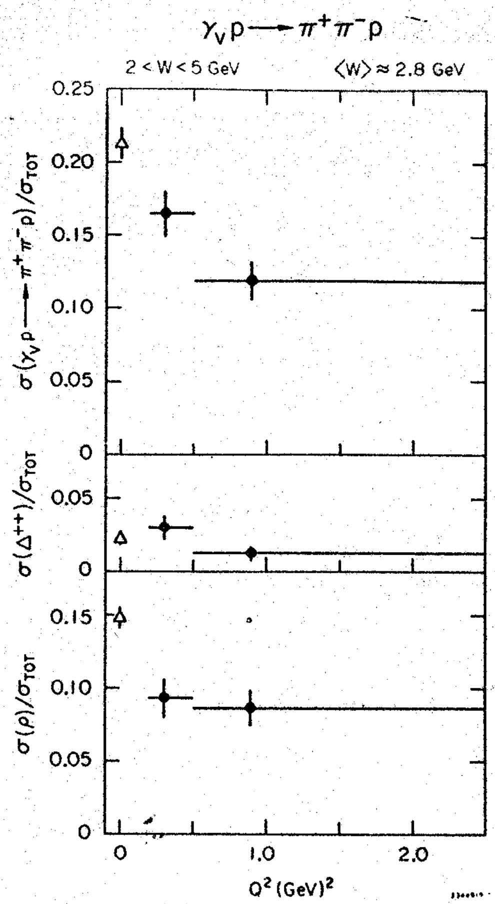

FIG. 14

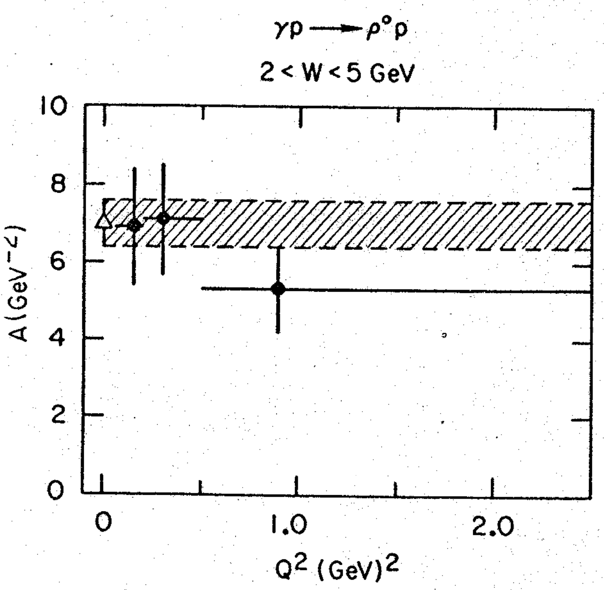

FIG. 15

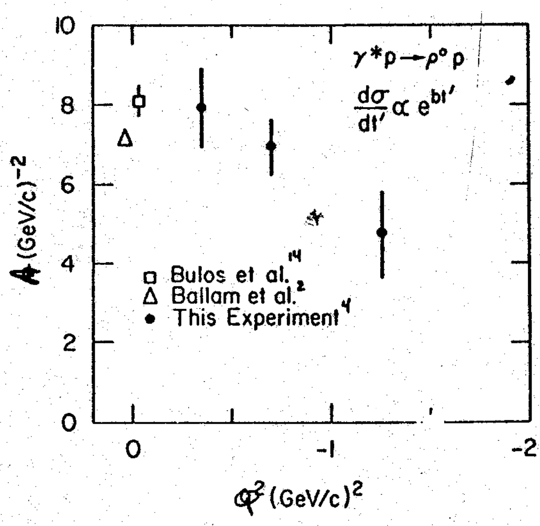

FIG. 16

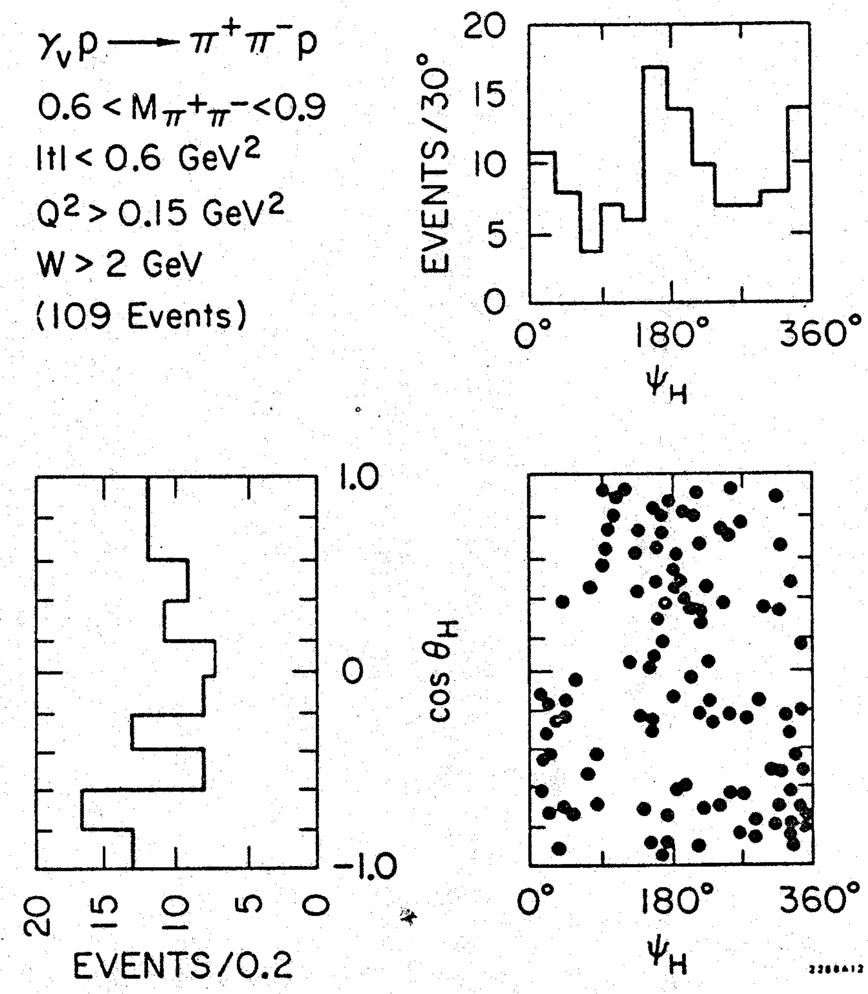

$\gamma_V p \longrightarrow \pi^+\pi^- p$
$0.6 < M_{\pi^+\pi^-} < 0.9$
$|t| < 0.6\ GeV^2$
$Q^2 > 0.15\ GeV^2$
$W > 2\ GeV$
(109 Events)
EVENTS/30°
20
15
10
5
0
0°
180°
360°
ψ_H
$\cos\theta_H$
1.0
0
-1.0
20
15
10
5
0
EVENTS/0.2

FIG: 17

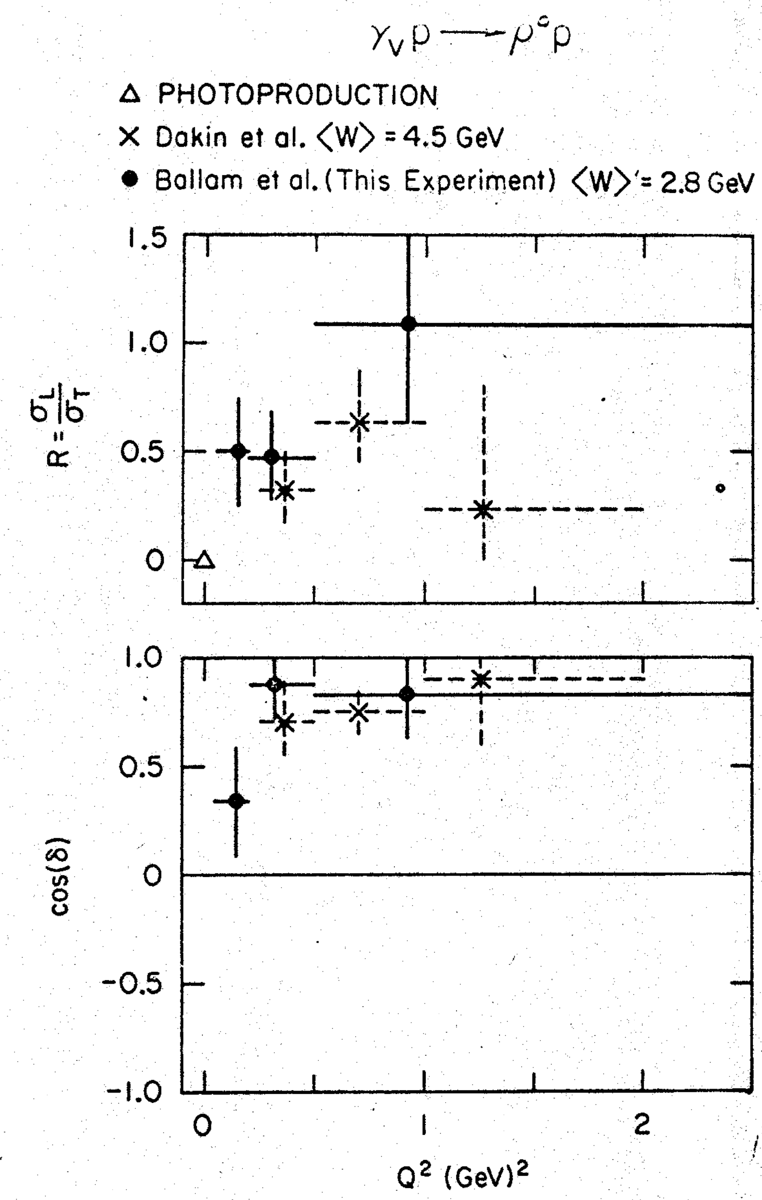

$\gamma_V p \longrightarrow \rho^\circ p$
△ PHOTOPRODUCTION
× Dakin et al. ⟨W⟩ = 4.5 GeV
● Ballam et al. (This Experiment) ⟨W⟩ = 2.8 GeV
$R = \frac{\sigma_L}{\sigma_T}$
1.5
1.0
0.5
0
$\cos(\delta)$
-0.5
-1.0
1
2
$Q^2\ (GeV)^2$

FIG. 18

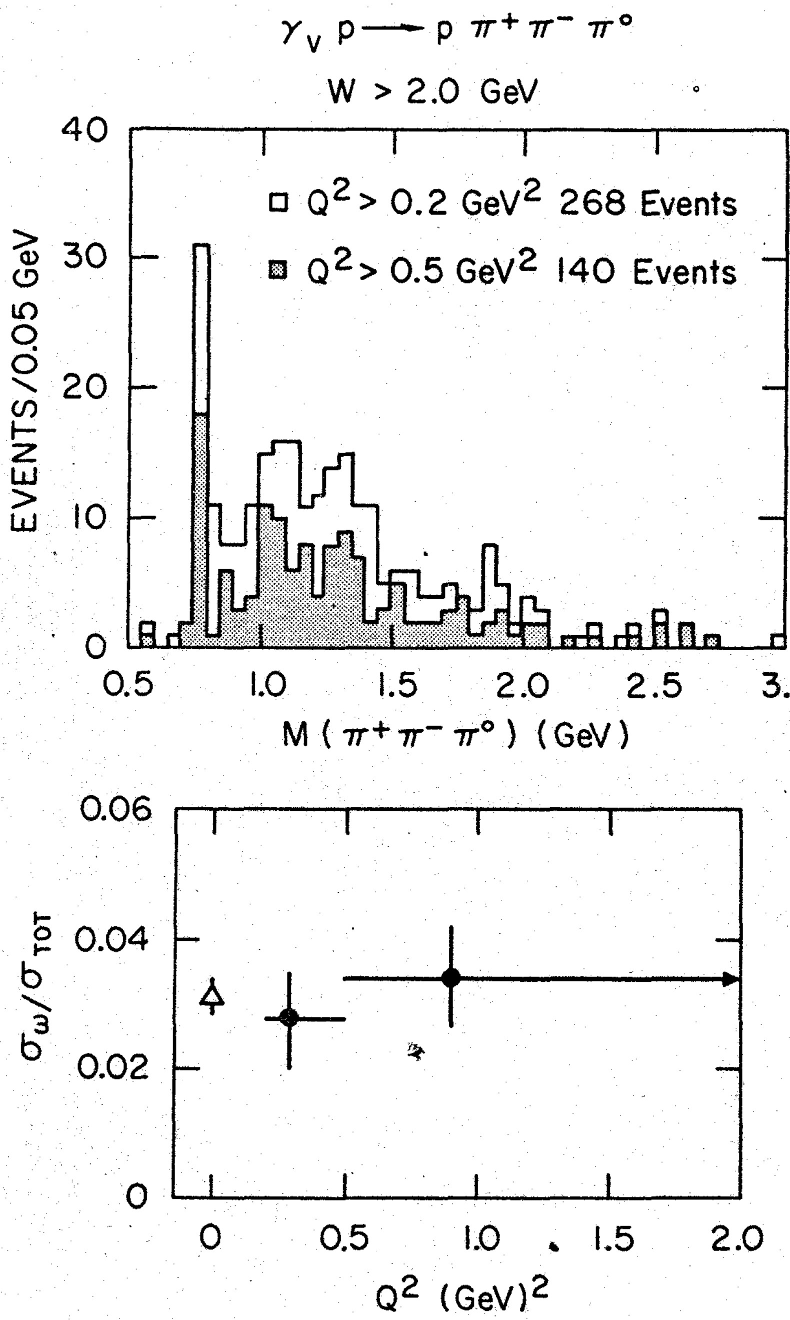
$\gamma_V\, p \longrightarrow p\, \pi^+ \pi^- \pi^\circ$
W > 2.0 GeV
$Q^2 > 0.2\ GeV^2$ 268 Events
$Q^2 > 0.5\ GeV^2$ 140 Events
EVENTS/0.05 GeV
40
30
20
10
0
0.5
1.0
1.5
2.0
2.5
3.0
$M(\pi^+ \pi^- \pi^\circ)$ (GeV)
$\sigma_\omega/\sigma_{TOT}$
0.06
0.04
0.02
0
0
0.5
1.0
1.5
2.0
$Q^2\ (GeV)^2$

FIG. 19

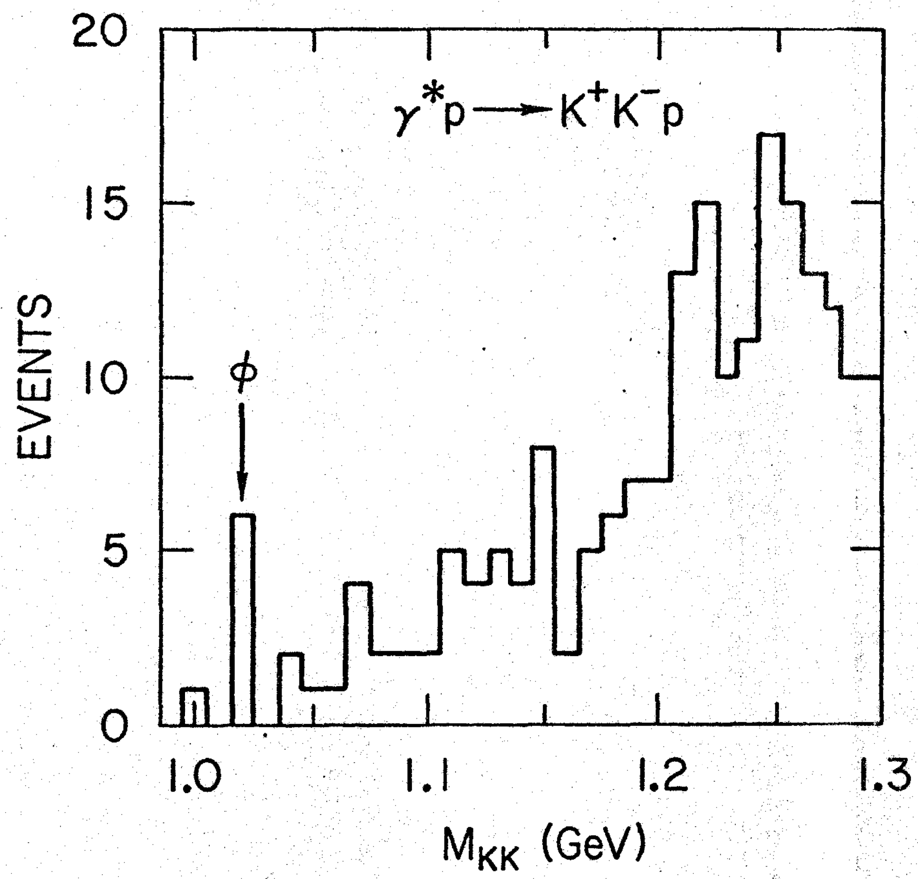
$\gamma^* p \longrightarrow K^+ K^- p$
ϕ
EVENTS
20
15
10
5
0
1.0
1.1
1.2
1.3
M_{KK} (GeV)

FIG. 20

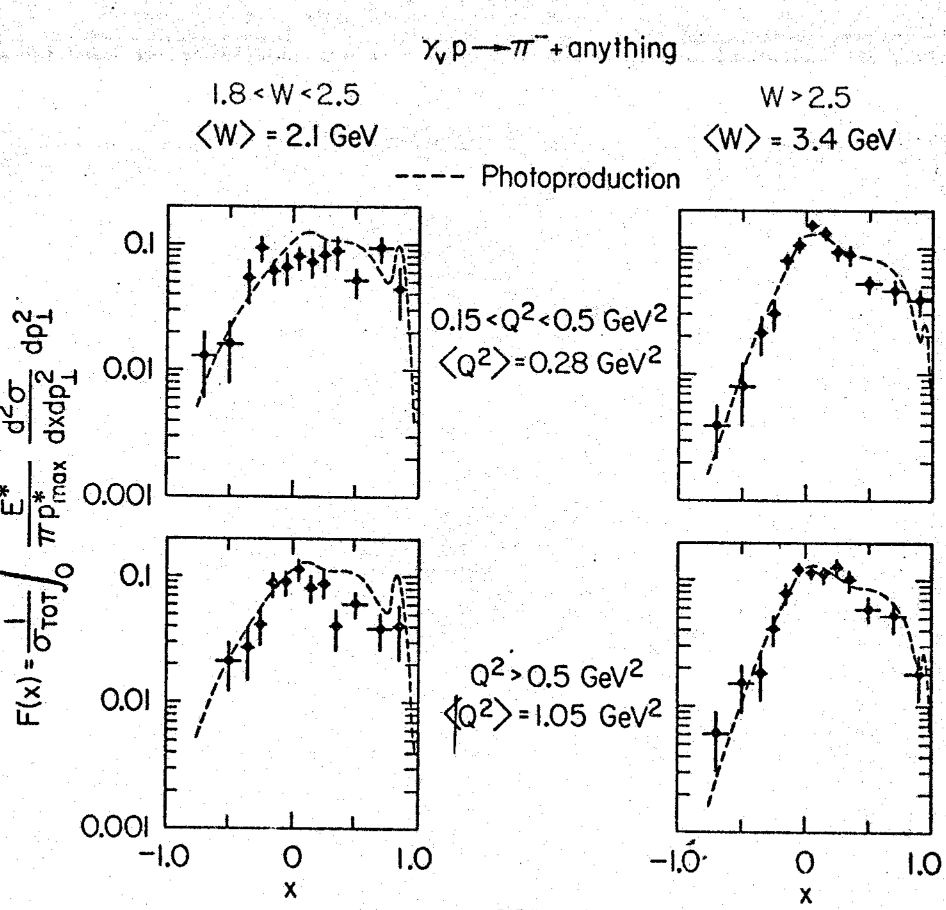
$\gamma_v p \to \pi^- +$ anything
1.8 < W < 2.5
⟨W⟩ = 2.1 GeV
W > 2.5
⟨W⟩ = 3.4 GeV
---- Photoproduction
0.15 < Q² < 0.5 GeV²
⟨Q²⟩ = 0.28 GeV²
Q² > 0.5 GeV²
⟨Q²⟩ = 1.05 GeV²
F(x) = 1/σ_TOT ∫₀^∞ E*/(π p*_max) d²σ/(dx dp⊥²) dp⊥²
0.1
0.01
0.001
−1.0
0
1.0
x

FIG. 21

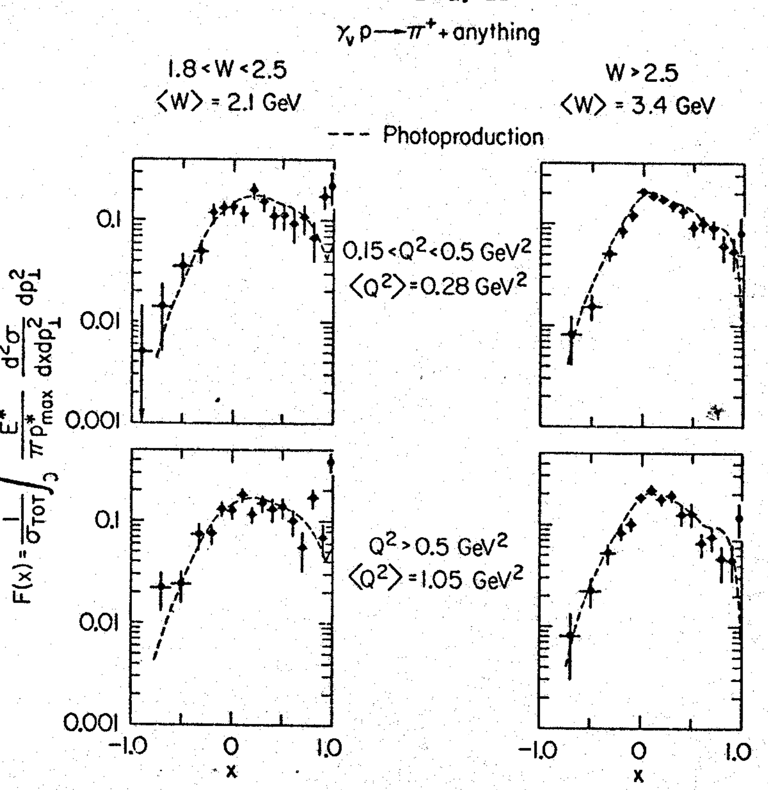
$\gamma_v p \to \pi^+ +$ anything
1.8 < W < 2.5
⟨W⟩ = 2.1 GeV
W > 2.5
⟨W⟩ = 3.4 GeV
--- Photoproduction
0.15 < Q² < 0.5 GeV²
⟨Q²⟩ = 0.28 GeV²
Q² > 0.5 GeV²
⟨Q²⟩ = 1.05 GeV²
F(x) = 1/σ_TOT ∫₀^∞ E*/(π p*_max) d²σ/(dx dp⊥²) dp⊥²
0.1
0.01
0.001
−1.0
0
1.0
x

FIG. 22